JOURNAL OF GEOPHYSICAL RESEARCH, VOL. 105, NO. B3, PAGES 6043–6056, MARCH 10, 2000

Gravitational stability of three-dimensional stratovolcano edifices

Mark E. Reid, Sarah B. Christian, and Dianne L. Brien
U.S. Geological Survey, Menlo Park, California

Abstract. Catastrophic flank collapses have occurred at many stratovolcanoes worldwide. We present a three-dimensional (3-D) slope stability analysis for assessing and quantifying both the locations of minimum edifice stability and the expected volumes of potential failure. Our approach can search the materials underlying a topographic surface, represented as a digital elevation model (DEM), and determine the relative stability of all parts of the edifice. Our 3-D extension of *Bishop*'s [1955] simplified limit-equilibrium analysis incorporates spherical failure surfaces, variable material properties, pore fluid pressures, and earthquake shaking. Although a variety of processes can trigger collapse, we focus here on gravitationally induced instability. Even homogeneous rock properties strongly influence the depth and volume of the least stable potential failure. For large failures in complex topography, patterns of potential instability do not mimic local ground surface slope alone. The May 18, 1980, catastrophic failure of the north flank of Mount St. Helens provides the best documented case history to test our method. Using the undeformed edifice topography of Mount St. Helens in an analysis of dry, static slope stability with homogeneous materials, as might be conducted in a precollapse hazard analysis, our method identified the northwest flank as the least stable region, although the north flank stability was within 5% of the minimum. Using estimates of the conditions that existed 2 days prior to collapse, including deformed topography with a north flank bulge and combined pore pressure and earthquake shaking effects, we obtained good estimates of the actual failure location and volume. Our method can provide estimates of initial failure volume and location to aid in assessing downslope or downstream hazards.

1. Introduction

Catastrophic flank collapse has drastically altered many composite volcano or stratovolcano edifices around the world [*Ui*, 1983; *Siebert*, 1984; *Siebert et al*., 1987; *McGuire*, 1996]. A dramatic modern example is the massive failure of Mount St. Helens in 1980 [*Voight et al*., 1983]. These large collapses, commonly involving >0.1 km^3 of material, often generate debris avalanches that may subsequently mobilize into debris flows, thereby creating major hazards both on the edifice itself and in areas far downslope or downstream. A wide variety of processes tend to destabilize edifices [*Voight and Elsworth*, 1997]; collapses can be caused by volcano-specific effects such as magma intrusion [*Elsworth and Voight*, 1995], hydrothermal alteration [*Lopez and Williams*, 1993], and thermal pressurization of pore fluids [*Reid*, 1994, 1995; *Elsworth and Voight*, 1995; *Day*, 1996], or they may occur in response to more commonly recognized slope destabilizing effects such as elevated pore fluid pressures or earthquake shaking. Although large collapses have not been identified at all stratovolcanoes, they are commonplace in some volcanic terrain [*MacLeod*, 1989], and multiple failures have occurred at some edifices [*Beget and Kienle*, 1992].

Hazard analyses of these phenomena typically rely on one or more of four techniques: (1) historical and prehistorical geologic investigations of previous events [*Crandell and Mullineaux*, 1975]; (2) comparison to analogous events at other volcanoes [*Siebert et al*., 1987]; (3) monitoring of volcanic unrest [*McGuire*, 1995; *Tilling*, 1995]; and (4) general or site-specific modeling of the physical processes [*Voight et al*., 1983; *Voight and Sousa*, 1994; *Voight and Elsworth*, 1997]. However, conditions can change within a volcanic edifice, and future collapse events may differ significantly from past events. Moreover, collapse may occur rather unexpectedly; for example, the precise timing of collapse at Mount St. Helens in 1980 was unanticipated [*Voight et al*., 1983].

Physically based mechanical models, developed for geotechnical analyses, provide tools for assessing and quantifying slope instability under a wide variety of conditions. For homogeneous materials and uniform pore fluid pressures, simple one-dimensional force balance analyses predict that steeper slopes are more unstable [*Lambe and Whitman*, 1969]; thus patterns of instability generally tend to mimic topographic slope. More complex methods have been developed to analyze the stability of two-dimensional (2-D) and three-dimensional (3-D) slopes. For simple hillslope shapes, 2-D slope stability analyses typically provide results indicating a lower stability than 3-D methods, but differences between the two methods are often within 10–20% [*Hovland*, 1977; *Xing*, 1988; *Duncan*, 1996]. However, 2-D methods cannot accurately estimate potential failure volumes in a 3-D hillslope. Moreover, complex topography can be difficult to represent adequately with 2-D stability methods. Various methods of 3-D slope stability analysis have been developed to better analyze the stability of 3-D landforms [*Baligh and Azzouz*, 1975; *Hovland*, 1977; *Chen and Chameau*, 1982; *Gens et al*., 1988; *Hungr*, 1987; *Lam and Fredlund*, 1993]. A cone with complex surface topography, typical of many vol-

Paper number 1999JB900310.

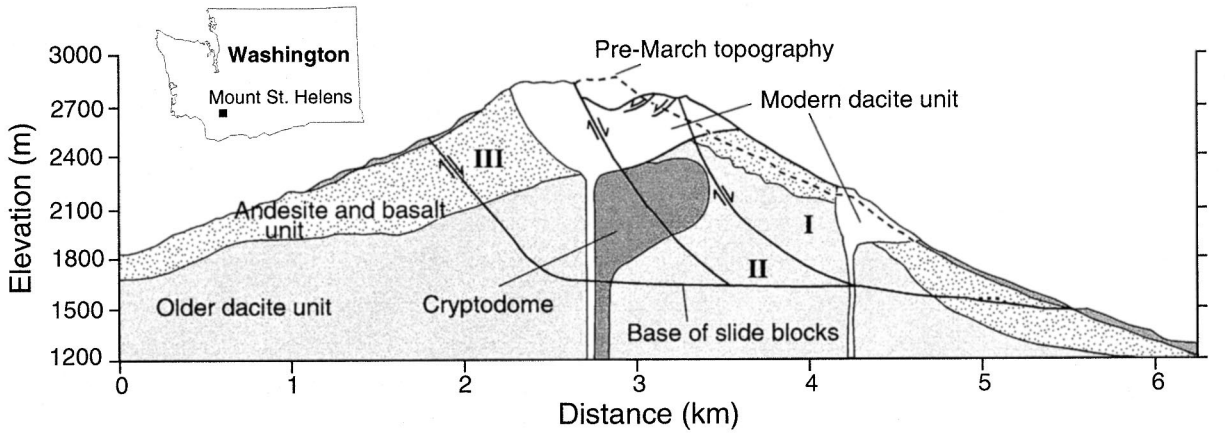

Figure 1. Cross section through precollapse Mount St. Helens showing failure surfaces defining slide block I and subsequent blocks II and III (adapted from *Glicken* [1996]).

cano edifices, should influence both the magnitude and patterns of instability.

Herein, we present a 3-D "method of columns" slope stability analysis that can search a landscape represented as a digital elevation model (DEM) and determine the relative stability of all parts of the 3-D medium underlying the topography. Our analysis uses a 3-D extension of *Bishop*'s [1955] 2-D simplified limit-equilibrium analysis, and it can incorporate some effects of pore fluid pressures and earthquake shaking. Our method can estimate both the locations of minimum stability and the expected potential failure volumes. Although 3-D stability methods have been presented elsewhere [*Hungr et al*., 1989] and 2-D methods have been used to search DEMs for unstable slopes [*Miller*, 1995], our method combines the two approaches. The promise of stability modeling is often tempered by the lack of critical information about the interior of most stratovolcano edifices, including poorly understood distributions of material properties and internal structures, inadequate knowledge of pore fluid pressures, and unpredictable, transient earthquake and magmatic effects. However, ground surface topography is well known for many stratovolcano edifices. Here we focus on general assessments of gravitationally induced instability primarily influenced by topography and ignore poorly constrained spatial variability in rock properties.

We use our analysis method to examine how uniform changes in rock properties and changes in volcano morphology modify slope stability. We then apply our approach to the preeruption topography of Mount St. Helens to examine whether our knowledge of topography alone would have provided significant insight into the location and size of the May 18, 1980, catastrophic failure. Mount St. Helens provides a well-documented example of a large collapse, and as such it provides a good test case for examining our methods. Although its collapse was clearly influenced by magma intrusion, we are particularly interested in the question: Can topography alone be used to aid in precollapse hazard analyses? We also examine the stability of the deformed Mount St. Helens edifice as it existed 2 days prior to collapse. Finally, we discuss how our methods for estimating potential failure volume and location might help assess the magnitude and reach of debris avalanches and debris flows mobilized from large collapses. The devastating effects from these phenomena can extend great distances downslope or downstream from the edifice and represent one of the greatest hazards at many stratovolcanoes [*Pierson*, 1989; *Siebert*, 1996].

2. Mechanical Analysis of Stability

Geotechnical investigations of gravitationally induced slope failure typically use two methods to examine slope stability: deformation-stress analysis and limit-equilibrium analysis [*Morgenstern*, 1992; *Duncan*, 1996]. Limit-equilibrium analysis examines the overall force and/or moment balance of a rigid mass potentially sliding along a predetermined failure surface. It uses the factor of safety, F, defined as the ratio of available shear strength to shear stress required for equilibrium, to predict stability. Limiting equilibrium results when $F = 1$; values of $F < 1$ indicate that slope failure theoretically occurs. Using these methods, the stability of any potential failure surface can be evaluated. Because we are interested in assessing where failure would occur in a 3-D volcano edifice, we first identify an appropriate 3-D failure mode and then use the 3-D limit-equilibrium analysis described below.

2.1. Volcano Slope Failure Mode

A wide variety of slope failures occur on volcano edifices, ranging from small rockfalls to massive collapses. Rock failure mechanisms often involve planar or wedge-shaped failure surfaces along discontinuities such as faults, joints, or weak bedding layers. However, rock failure may also be arcuate if discontinuities are closely spaced [*Hoek and Bray*, 1981]. The influence of discontinuities is often one of scale; small discontinuities may not influence the shape of large failures. *Dieterich* [1988] and *Iverson* [1991, 1992, 1995] assumed translational movement of a single wedge in their analyses of gigantic failures on the shield volcanoes of the Hawaiian islands. *Voight and Elsworth* [1997] used this sliding wedge failure mechanism for both shield and stratovolcanoes. In earlier work, *Voight et al*. [1983] and *Glicken* [1996] assumed arcuate failure surfaces for the massive 1980 Mount St. Helens slope failure (Figure 1).

In our mechanical analyses we assume an arcuate failure surface defined by the intersection of a sphere with the 3-D materials underlying topography (Figure 2). We selected this failure geometry for two reasons.

1. We are primarily interested in stratovolcano edifice failures with large volumes, such as the 1980 Mount St. Helens

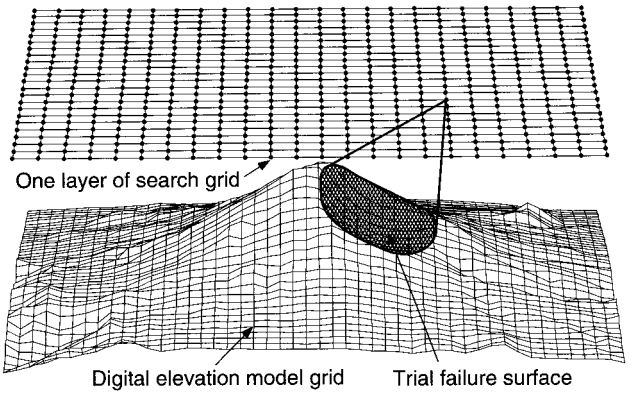

Figure 2. Digital elevation model of a volcanic edifice with one layer of search grid points. Mass from a trial failure has been removed from the topography to show the failure surface. Stability is computed using the vertical columns intersected by the trial failure surface.

failure, rather than more modest sized rockslides. Most large stratovolcano failures have volumes between 0.1 and 20 km^3 [*Siebert et al*., 1987; *Siebert*, 1996], and the final amphitheater shape of many collapses may be due to a variety of gravitational and eruptive processes. However, an arcuate failure surface was interpreted for the initial sliding blocks at Mount St. Helens [*Voight et al*., 1983], as well as for Bandai and Bezymianny volcanoes [*Voight and Elsworth*, 1997]. Moreover, the arcuate morphology of most postfailure stratovolcano edifices not affected by magmatic or phreatic eruptions, such as Mayu-yama in Japan [*Siebert et al*., 1987], indicates this failure surface geometry.

2. Typically, little is known about the location of major discontinuities within an edifice prior to failure. As a result, we ignore any possible discontinuities that might lead to translational block sliding and focus instead on the potential effects of topography on slope instability. A spherical potential failure surface represents the simplest 3-D geometry unconstrained by internal structures.

2.2. Three-Dimensional Slope Stability

We use a 3-D extension of *Bishop*'s [1955] simplified 2-D method of slices for limit-equilibrium analysis. Similar 3-D methods of columns have been described by other authors [*Hungr*, 1987; *Ugai*, 1988; *Hungr et al*., 1989; *Lam and Fredlund*, 1993]. Bishop's 2-D simplified method is often used for geotechnical engineering calculations, and it provides quite accurate results, typically within a few percent of more rigorous, but cumbersome, 2-D methods [*Whitman and Bailey*, 1967; *Fredlund and Krahn*, 1977; *Duncan and Wright*, 1980]. *Hungr et al*. [1989] and *Lam and Fredlund* [1993] have shown that the 3-D extension of Bishop's simplified method also provides quite accurate results for 3-D arcuate failures. Our method is implemented in a computer code named SCOOPS. This code performs 3-D limit-equilibrium computations in a manner similar to, and with the basic assumptions used by *Hungr* [1987], but adds the capability of computing slope stability throughout a digital representation of a landscape.

Bishop's [1955] limit-equilibrium analysis assumes that the average shear resistance τ, acting on a potential failure surface, is given by the Coulomb-Terzaghi failure rule:

$$\tau = c + (\sigma_n - u) \tan \phi, \tag{1}$$

where c is cohesion, σ_n is the total normal stress acting on the failure surface, u is pore fluid pressure on the failure surface, and ϕ is the angle of internal friction. A number of researchers advocate the use of this rule for the strength of closely jointed rock [*Jaeger and Cook*, 1979; *Hoek and Bray*, 1981]. Shear stress is equal to shear resistance at failure. Many limit-equilibrium methods specify that a constant proportion $1/F$ of the available shear strength resists the shear stress. Thus the average resisting shear force at equilibrium, S, is

$$S = (1/A) \int_A [(\tau A)/F]\, dA, \tag{2}$$

where A is the total failure surface area.

To estimate the forces acting on each part of a potential failure surface, we assume a spherical failure surface with the solid failure domain divided into 3-D vertical columns. This allows easy integration with a digital elevation model (DEM), a spatial array of elevations representing the ground surface topography. Our analysis begins by defining an arbitrary point in space above the DEM. This point forms the center of a spherical trial failure surface with radius r, and we then determine the DEM columns (both full and partial) contained within that surface (Figure 2). Column shape is controlled by the DEM spacing and a partial column contains two or more DEM nodes. The segment of the spherical failure surface intersecting each column is approximated locally as a plane dipping at angle θ. Given a radius r, the slope of the failure surface through the center of each column is computed by taking the partial derivatives ($\partial z/\partial x$ and $\partial z/\partial y$) of the equation for the spherical failure surface:

$$r^2 = x^2 + y^2 + z^2, \tag{3}$$

where x, y, and z are orthogonal coordinates relative to the sphere center. The true dip of the failure surface, θ, and the apparent dip in the direction of slide movement, α, are computed using

$$\theta = \cos^{-1} [1/\sqrt{1 + (\partial z/\partial x)^2 + (\partial z/\partial y)^2}] \tag{4}$$

$$\alpha = \tan^{-1} [(\partial z/\partial x) \cos \beta + (\partial z/\partial y) \sin \beta], \tag{5}$$

where β is the azimuthal angle of the slide movement direction, measured counterclockwise from zero in the positive x direction.

To obtain a factor of safety for this trial failure surface, our 3-D extension of *Bishop*'s [1955] simplified method first computes the vertical force equilibrium acting on the failure surface intersecting each column:

$$W = N_z + S_z = P \cos \theta + \left[\frac{cA_C}{F} + \frac{(P - uA_C) \tan \phi}{F} \right] \sin \alpha, \tag{6}$$

where W is the weight of the column above the failure surface, N_z is the vertical component of the normal force acting on the failure surface, S_z is the vertical component of the shear force (obtained from equation (2)) acting on the failure surface, P is the normal force acting on the failure surface, and A_c is the area of the failure surface intersecting the column. We approximate the failure surface at the base of the column by a plane that intersects the spherical surface at the midpoint of the column. Note that the vertical component of the normal force is resolved with respect to the true dip of the trial failure

surface, θ. The shear force acts parallel to the apparent dip in the direction of potential sliding, so the vertical component of this force is resolved with respect to α. Vertical shear between individual columns is ignored.

We compute weight W by first determining the volume V of each column (partial or full) above the failure surface using an approximation for prismoids:

$$V = 1/6\Delta x(S_0 + 4S_1 + S_2), \tag{7}$$

where Δx represents the DEM grid spacing, S_0 and S_2 are the surface areas of the two parallel sides of the column, and S_1 is the surface area of a vertical cross section through the middle of the column. Then,

$$W = V\gamma_t, \tag{8}$$

where γ_t is total (rock plus fluid) unit weight. If the column contains more than one material with different properties, volume and weight are appropriately integrated above the failure surface.

The normal force P acting on the trial failure surface can be found from (6):

$$P = \left(W + \frac{uA_C \tan \phi \sin \alpha}{F} - \frac{cA_C \sin \alpha}{F} \right) \Big/ m_\alpha, \tag{9a}$$

where

$$m_\alpha = \cos \theta + \frac{\tan \phi \sin \alpha}{F}. \tag{9b}$$

Horizontal force equilibrium between columns is not explicitly determined; thus our method is mechanically quasi-3-D.

The global moment equilibrium for all columns, $\sum M_o$, for rotation about the axis through the center of the trial failure surface sphere equals zero, and is defined by

$$\sum M_o = 0 = \sum R \frac{(cA_C + (P - uA_C) \tan \phi)}{F} - \sum Wa - \sum Wke, \tag{10}$$

where R is the resisting force moment arm (equal to the failure surface radius), a is the vertical driving force moment arm (equal to $R \sin \alpha$), k is the horizontal pseudo-acceleration from earthquake shaking (expressed as a fraction of g, the magnitude of gravitational acceleration), and e is the horizontal driving force moment arm (equal to the vertical distance from the center of the column to the elevation of the axis of rotation). The destabilizing effects of earthquake shaking are reduced to a pseudo-static horizontal force [*Seed and Martin*, 1966]. With no earthquake shaking, k equals zero. Using (10), a factor of safety F against rotation can then be defined by

$$F = \frac{\sum R(cA_C + (P - uA_C) \tan \phi)}{\sum W(R \sin \alpha + ke)}. \tag{11}$$

Substituting in P from (9a) gives

$$F = \frac{\sum R(cA_C \cos \theta + (W - uA_C \cos \theta) \tan \phi)/m_\alpha}{\sum W(R \sin \alpha + ke)}. \tag{12}$$

Determining the pore fluid pressure acting on each column can be difficult owing to complex gravity-driven or thermally driven groundwater flow within an edifice that would create spatially variable pore pressures. *Bishop* [1955] suggested using the pore pressure ratio r_u as a method to account for relatively uniform pore pressure effects:

$$r_u = u/(\gamma_t Z), \tag{13}$$

where Z is the vertical distance from the failure surface to the ground surface. Dry materials have an r_u of zero. Using the pore pressure ratio, (12) becomes

$$F = \frac{\sum R[cA_C \cos \theta + W(1 - r_u) \tan \phi]/m_\alpha}{\sum W(R \sin \alpha + ke)}. \tag{14}$$

The overall factor of safety, F, as defined by (14), must be found by iteration because the resisting force is a function of F as shown by (9b). Convergence can be sensitive to the selection of an initial value of F, particularly for a steep apparent slip surface oriented against rotation (negative α) near the toe of the potential failure. We compute an initial F using a method similar to that proposed by *Chowdhury and Zhang* [1990] for 2-D analyses. If there are columns within the trial surface having negative values of α, then

$$\text{initial } F = 1 + |\tan \alpha_i \tan \phi_i|, \tag{15}$$

where i designates the column having the largest negative α. If all columns have a positive α, then we use an initial F of one.

Our implementation in SCOOPS includes several aspects critical for assessing the stability of stratovolcano edifices. Spatially variable material properties (strength and density) can be incorporated in different internal layers beneath the surface topography; this feature is not used in our homogeneous assessments. The uniform pseudo-static earthquake term and the pore pressure ratio are large simplifications of the actual processes acting in an edifice. However, in the absence of detailed knowledge, they allow us to investigate the relative importance of these processes on edifice stability.

2.3. Determining the Least Stable Areas

Determining the patterns of stability of a volcano edifice entails finding the trial failure surface with the lowest factor of safety (critical surface) affecting each section of the edifice. This requires a thorough search of all possible failure surfaces throughout the DEM. For 2-D slope stability analyses, some researchers have employed variational or optimization techniques to find critical surfaces from a potentially infinite number of trial surfaces [*Duncan*, 1996], but most analyses still rely on some trial and error searching through a subset of the potential surfaces. We are interested in evaluating potential failure surfaces having a wide range of volumes (or areas) that affect the 3-D medium underlying irregular topography. These conditions may result in many local factor of safety minima; optimization techniques are not generally able to determine all local minima.

Because of these issues, our search methodology takes a different approach. First, we define either a range of failure volumes or of failure areas to be evaluated. This range can be wide, allowing a thorough search, or it can be restricted, allowing only particular failure volumes (or areas) of interest. We then systematically search through the DEM using a 3-D orthogonal search grid of points located above the DEM (Figure 2). Each point in this search grid represents the center of rotation of a set of spherical trial failure surfaces with different radii. If the intersection of the spherical surface and the ma-

terials underlying the DEM meets the search criteria (i.e., creates a potential slide mass in the appropriate volume or area range), then a factor of safety is computed for this trial surface. The initial radius of the potential failure surface is selected to create a failure volume between the lower volume (or area) limit and the lower volume (or area) plus a tolerance. Then the radius is incrementally increased by a defined amount until the failure mass exceeds the maximum volume (or area) limit, or until it intersects the edge of the DEM. It is possible that a given radius may create multiple potential failure surfaces affecting the DEM as a result of uneven topography, and we test each surface that meets the volume (or area) criteria.

In two dimensions, movement during failure is only possible in one plane, usually in the downslope direction. For a given potential failure affecting a 3-D medium we identify an overall topographic "fall line," defined as the sum of the surface slope vectors for all columns contained in the failure volume. In a 3-D medium, actual movement on a potential failure surface is possible in many directions. Because of variations in topography or material properties the least stable movement direction may not necessarily be directly down the fall line. We always compute the factor of safety for movement in the overall fall line direction, but we can also compute F for other specified slip directions with initial movement to either side of the fall line direction (this alters the apparent dip in the direction of slide movement, α). After evaluating the possible failures at a given search grid point, our analysis moves to the next point and repeats the same process until all points in the search grid have been assessed.

To perform a thorough search, we can manipulate the limits of the search grid, the search grid spacing, the spherical radius increment, and the directions of slip movement. Some trial and error testing is required to ensure an exhaustive search. In addition to the search criteria, two other aspects affect the quality of the numerical results. The DEM itself must have sufficient resolution to portray topographic conditions that affect stability. For large failures (>0.1 km^3) we have found that a DEM with 100-m cells usually provides factor of safety results within 1% of DEMs with 30-m cells. Finally, there must be a sufficient number of columns included in the trial failure surface to provide adequate numerical precision. We have found that a trial failure composed of at least 200 columns produces both factor of safety and potential failure volume results within 1% of failures represented by thousands of columns. Using fewer than 200 columns can result in low computed volumes. Thus, producing a precise stability analysis requires three conditions: (1) conducting a reasonably thorough search of possible trial failure surfaces, (2) using a DEM with sufficient topographic resolution, and (3) ensuring that enough columns are included in each trial surface.

Upon completion of this process, every DEM grid point of interest will have been included in some trial failures. The minimum stability at each DEM grid point is determined by the lowest factor of safety of any trial surface (critical surface) that includes that DEM grid point. We also determine the volume associated with the critical surface at each DEM point (critical volume). We can then create a map of relative edifice stability by portraying the lowest factor of safety at each DEM grid point.

We compared our 3-D limit-equilibrium method with other published 3-D analyses. Using homogeneous, conical edifices, we determined the failure surface having the minimum factor of safety for the entire cone and its associated volume; different tests covered a range of material properties (including $\phi = 0$ cases), slope angles (between 26° and 70°), pore fluid pressures, and earthquake shaking effects. We then compared our results against those from an analytical solution for a 3-D log spiral failure surface [*Baker and Leshchinsky*, 1987] that can be closely approximated by a spherical failure surface, and from CLARA, a commercially available stability package that also uses a 3-D version of Bishop's simplified limit-equilibrium analysis [*Hungr et al*., 1989]. Our search methods were able to determine the critical surface factor of safety within 1–2% and critical volume within 1–5% of the other methods without specifying a failure surface a priori. Given a fixed failure surface, our factor of safety results differed by $<1\%$ from results using CLARA.

Table 1. Range of Volcanic Rock Properties

Rock Character	γ, kN/m^3	ϕ, deg	c, kPa	λ^*
Very strong (unfractured)	24	40	10,000	0.5
Strong (fractured)	24	40	1,000	0.05
Weak	19	27	500	0.05
Very weak	19	15	10	0.002

Data are from *Jaeger and Cook* [1979], *Voight et al*. [1983], and *Watters and Delahaut* [1995].
*For $H = 1000$ m.

3. Stability of Uniform 3-D Cones

Before proceeding with a stability analysis of a volcanic edifice with irregular topography, the potential effects of rock properties and slope morphology must be understood. Coulomb strength and, to a lesser extent, rock density are fundamental properties strongly influencing gravitationally induced slope instability. Stratovolcano edifices can be extremely heterogeneous, containing rocks or unconsolidated materials with a wide range in properties. Fresh andesite or dacite may be relatively strong with high frictional strength, large cohesion (or tensile strength), and high density. Fracturing may reduce cohesion. Pyroclastic units or hydrothermally altered rocks may be much weaker and have lower densities. Table 1 shows some values characteristic of the range in properties for volcanic rocks.

For a given cone, weaker materials lead to less stable slopes. Weak layers or structural discontinuities can clearly influence potential failure location and volume. However, uniform rock strength and density can also affect the location of the critical failure surface, and corresponding failure depth and volume. Within a homogeneous cone having a specified slope, the location of the critical failure surface is controlled by the dimensionless ratio:

$$\lambda = c/(\gamma H \tan \phi), \tag{16}$$

where H is the height of the cone. Similar dimensionless cohesive to frictional strength ratios have been defined by other researchers [*Janbu*, 1954; *Hoek and Bray*, 1981; *Baker and Leshchinsky*, 1987]. Cones having the same geometry and the same value of λ will have the same critical potential failure surfaces and corresponding critical volumes, even though they may have greatly different factors of safety.

We used SCOOPS to examine the effect of λ on a homoge-

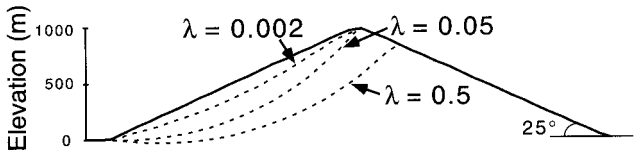

Figure 3. Least stable failure surface in a homogeneous, 25°, symmetric cone computed using different values of λ. Larger values of λ have deeper failure surfaces; λ is defined as the dimensionless ratio of cohesive to frictional strength $c/(\gamma H \tan \phi)$.

neous, 1000-m-high, 25° cone. Several noteworthy effects of λ relevant to edifice stability are illustrated in Table 1 and Figure 3.

1. Slopes with very different strengths can have the same λ. For example, both the strong, fractured rock and the weak rock shown in Table 1 have a λ of 0.05. This results in different stabilities for slopes having these two different sets of properties, but the same critical surface and volume.

2. Larger values of λ result in deeper failures with larger volumes.

3. Cohesion can vary over several orders of magnitude (more than the other rock properties listed in Table 1) and therefore can exert a strong influence on the location of the critical failure surface and volume. In a cohesionless material (λ = 0) the critical surface will extend along the slope surface [*Baker and Leshchinsky*, 1987], implying that, all else remaining equal, potential failures will be thin. Large values of cohesion lead to large λ values and can create deep critical surfaces that extend behind the peak of the cone. Note that very large values of λ (such as 0.5) with large cohesion would be unrealistic in most stratovolcano edifices.

4. Increases in frictional strength or density decrease the critical volume.

We also used our analysis method to examine the effects of variations in slope morphology on stability and failure volume. Figure 4 illustrates these effects for 1000-m-high uniform cones having different slope angles (20°, 30°, and 40°) and a λ of 0.05. Steeper cones tend to be less stable, as might be expected. However, the volumes associated with the critical failure surface decrease with increasing steepness. Nevertheless, in all three cases the volume of the critical failure remains ~11% of the total edifice volume because edifice volume decreases with increasing slope angle given the same height. In addition, we compared the stability of ridge-shaped and cone-shaped morphologies, both having a slope of 25° and a λ of 0.05. The critical 3-D failure in a straight ridge has a slightly lower factor of safety (by ~6%) and a volume about twice as large as the critical 3-D failure in a cone. Although this large difference in critical volumes between a ridge and a cone might be expected, it clearly demonstrates the need to account for the 3-D medium underlying topography when predicting critical failure volumes because a 2-D analysis would not distinguish between these two morphologies. Thus both slope angle and morphology can greatly affect slope stability and potential failure volume.

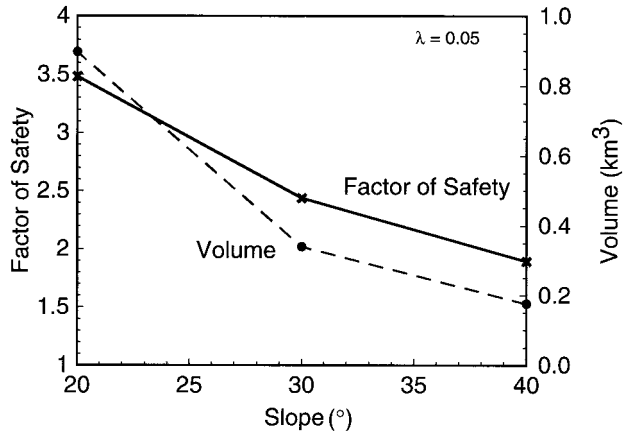

Figure 4. Changes in factor of safety and volume for the least stable failure surface in homogeneous symmetric cones having different slopes.

4. Application to Volcano Topography: Mount St. Helens

The well-documented, catastrophic debris avalanche at Mount St. Helens on May 18, 1980, provides an opportunity to examine the usefulness of our 3-D stability analysis. In March 1980 the north flank of Mount St. Helens began moving northward at the rate of several meters per day, creating a conspicuous bulge about 1.5 by 2 km in area [*Lipman et al*., 1981], apparently in response to shallow magma intrusion and associated rock dilation [*Voight et al*., 1983]. Finally, on May 18, in association with a magnitude 5.2 earthquake, the north flank failed rapidly and retrogressively in a series of large blocks shown in Figure 1, beginning with slide block I [*Voight*, 1981; *Voight et al*., 1983; *Glicken*, 1996]. The entire rockslide had an estimated volume of 2.3 km^3 and resulted in a heterogeneous debris avalanche deposit of about 2.8 km^3 [*Voight et al*., 1983]. Using the information provided by *Voight et al*. [1983] and *Glicken* [1996], in combination with the deformed topography, we estimate that the initial slide block I had a volume of about 0.8 km^3.

The precollapse slope stability of several surfaces within the north flank was analyzed by *Voight et al*. [1983] using a 2-D simplified Bishop's limit-equilibrium analysis. They concluded that both high pore fluid pressures and earthquake shaking were required to destabilize the deformed north flank. They also inferred that collapse was not entirely due to gravity acting on the edifice topography; shallow magma intrusion with accompanying mechanical and thermal effects destabilized the edifice [*Voight et al*., 1983]. On the basis of seismic analysis of the collapse event, *Kanamori et al*. [1984] proposed that the initial earthquake may have been the result of the landslide, rather than causing the landslide.

Given the wealth of data about Mount St. Helens, we can investigate how well our analysis method might have predicted precollapse edifice stability. Digital elevation models are available for both the predeformation topography and the deformed topography as it existed two days prior to collapse. Using these DEMs, we examined the stability of the undeformed edifice, as might be done in a hazards analysis, as well as changes in stability caused by edifice deformation. Our intent is not to simulate the actual Mount St. Helens collapse as did *Voight et al*. [1983]; a 3-D analysis of this event would require detailed 3-D knowledge of all the driving and resisting forces. Instead, we investigate, in retrospect, whether potential instability caused by gravity acting on topography could have

provided useful estimates of the locations and volumes of potential failures.

4.1. Mount St. Helens Edifice Properties

To assess 3-D edifice stability using our geotechnical approach, we must estimate ground surface topography, rock strength, rock density, pore fluid pressures, and earthquake shaking intensity. We obtained the undeformed edifice topography from the 1979 U.S. Geological Survey Mount St. Helens 30-m DEM and constructed the deformed edifice topography by combining a 5-m DEM of the north flank bulge based on May 16, 1980, aerial photography [*Jordan and Kieffer*, 1981] with the 1979 DEM for the remainder of the edifice. We then resampled both of these DEMs to construct 75-m and 100-m DEMs using cubic convolution in the GRID program of ARC/INFO [*Environmental Systems Research Institute* (*ESRI*), 1998]. Comparative tests on these DEMs indicated that a 100-m DEM provides sufficient resolution to accurately compute the stability of potential failures with a volume >0.1 km^3, so we used 100-m resampled DEMs for the following analyses.

Prior to the catastrophic failure of the Mount St. Helens edifice, detailed 3-D distributions of rock strength and density were unknown. Following the collapse, *Voight et al*. [1983] and *Glicken* [1996], aided by geologic sections described by *Hopson and Melson* [1982], reconstructed the internal geologic structure and presented four generalized units (Figure 1). Older dacite dome lavas and flank breccias, both fresh and hydrothermally altered, formed the core of the mountain. This unit was overlain by andesitic and basaltic lava flows and tephras. More modern dacites formed the Summit and Goat Rocks domes. All of these units were intruded by the dacitic cryptodome during 1980. Given this variety of materials, rock properties were very likely heterogeneous and anisotropic within the edifice and also probably varied significantly within geologic units. *Swanson et al*. [1995] suggested that weak older dome complexes beneath the north flank predisposed this area to failure. However, no large areas of potentially weak, hydrothermally altered rocks, such as those found at other nearby Cascade volcanoes such as Mount Rainier [*Crowley and Zimbleman*, 1997], were visible at Mount St. Helens prior to collapse. Thus rock properties at Mount St. Helens prior to collapse appeared more homogeneous than at other nearby stratovolcanoes.

Voight et al. [1983] presented physical properties measured on debris avalanche materials from the Mount St. Helens collapse. They conducted direct shear tests on small specimens of debris avalanche material and obtained angles of internal friction, ϕ, ranging between 38° and 44°, with an average of about 40°. Using a numerical model of dry block interactions in the precollapse Mount St. Helens edifice, *Paul et al*. [1987] estimated that north flank stability required $\phi \geq 27°$. *Voight et al*. [1983] estimated cohesion c for their stability analyses as varying between 0 and 10 bars (about 0 to 1000 kPa) and an average specific weight for the intact edifice rock of 2.4 g/cm^3. Given a precollapse water table near the edifice surface, *Voight et al*. [1983] estimated the pore pressure ratio, r_u, as 0.3, and given the strong ground motion associated with a $M \sim 5.2$ earthquake, they estimated the horizontal acceleration as about $0.2g$.

In our analyses we are interested in gravity-driven instability controlled by topography. Because spatial variations in material properties were poorly known prior to collapse at Mount St. Helens, we initially assumed a strong, homogeneous, precollapse edifice with the following properties: $\phi = 40°$; $c = 1000$ kPa; $\gamma = 24$ kN/m^3. We also examined the potentially destabilizing effects of pore fluid pressure using $r_u = 0.3$ and of earthquake shaking using $k = 0.2$, incorporating the values suggested by *Voight et al*. [1983]. Although these values are clearly simplistic, they allow us to examine relative changes in stability induced by these phenomena. We selected broad volume constraints that allowed any potential failure surfaces with volumes between 0.1 and 3.5 km^3. For each trial failure surface we computed the factor of safety for initial sliding motion in the direction of the overall topographic fall line and also for assumed initial motion 2° to either side of the fall line.

4.2. Undeformed Edifice

We first examined the 3-D stability of the undeformed Mount St. Helens edifice, as might be done in a precollapse hazard analysis. Elevation contours and ground surface slopes derived from the 100-m undeformed DEM are shown in Plate 1a. Although most of the undeformed edifice was remarkably symmetrical with slopes between 20° and 30°, concentrations of locally steeper areas (around 40°) existed on the west, north, and east flanks. Plate 1b illustrates the relative factor of safety, F_{rel}, for each DEM node of the dry edifice with no earthquake shaking. F_{rel} is portrayed instead of F because a map of F_{rel} is valid for any combination of parameters resulting in the same λ value. F_{rel} is defined as the computed factor of safety normalized by the minimum factor of safety for the entire edifice, F_{min}:

$$F_{\text{rel}} = F/F_{\text{min}}. \tag{17}$$

F_{rel} equals one for the global minimum factor of safety and represents the computed least stable region. Larger values of F_{rel} are relatively more stable. Note that F can be easily determined from F_{rel} by using equation (17). Plate 1b depicts the lowest F_{rel} at each DEM grid point of all trial surfaces that contained that DEM point; the map is a composite of the F_{rel} associated with the critical failure surface for each point in the DEM. Thus the map shows a pattern of overlapping critical surfaces; only the potential failure area defined by F_{min} will necessarily be completely outlined.

Given the undeformed edifice topography, F_{min} (or $F_{\text{rel}} = 1$) occurs on two different trial failure surfaces affecting the northwest part of the edifice (Plate 1b). Both have an F_{min} of $\sim$2.23. Regions with low F_{rel} also occur on the north and southeast flanks. Most of the upper edifice has a relative stability within 10% of F_{min}. The potential failure volume associated with F_{rel} at each DEM point is portrayed in Plate 1c. For the chosen material parameters, regions with low F_{rel} fall within the 0.1 and 3.5 km^3 volume constraints. The two volumes associated with the minimum relative factor of safety ($F_{\text{rel}} = 1$) are shown in Figure 5; one has a volume of $\sim$0.3 km^3 and the other $\sim$0.8 km^3. Two minimum surfaces are present because of topographic detail; the smaller volume reflects a localized area of consistently steeper slopes, whereas the larger volume represents the integration of a larger area of steeper slopes (Plate 1a). For the undeformed edifice, there is a general increase in critical volume (the volume associated with the critical potential failure surface at each DEM grid) with increasing factor of safety. Very large critical surfaces that encompass an entire volcano flank ($\sim$3–3.5 km^3) result in an F at least 25% greater than F_{min} (Figure 5). Note that Figure 5 portrays both the critical volumes shown in Plate 1c and the

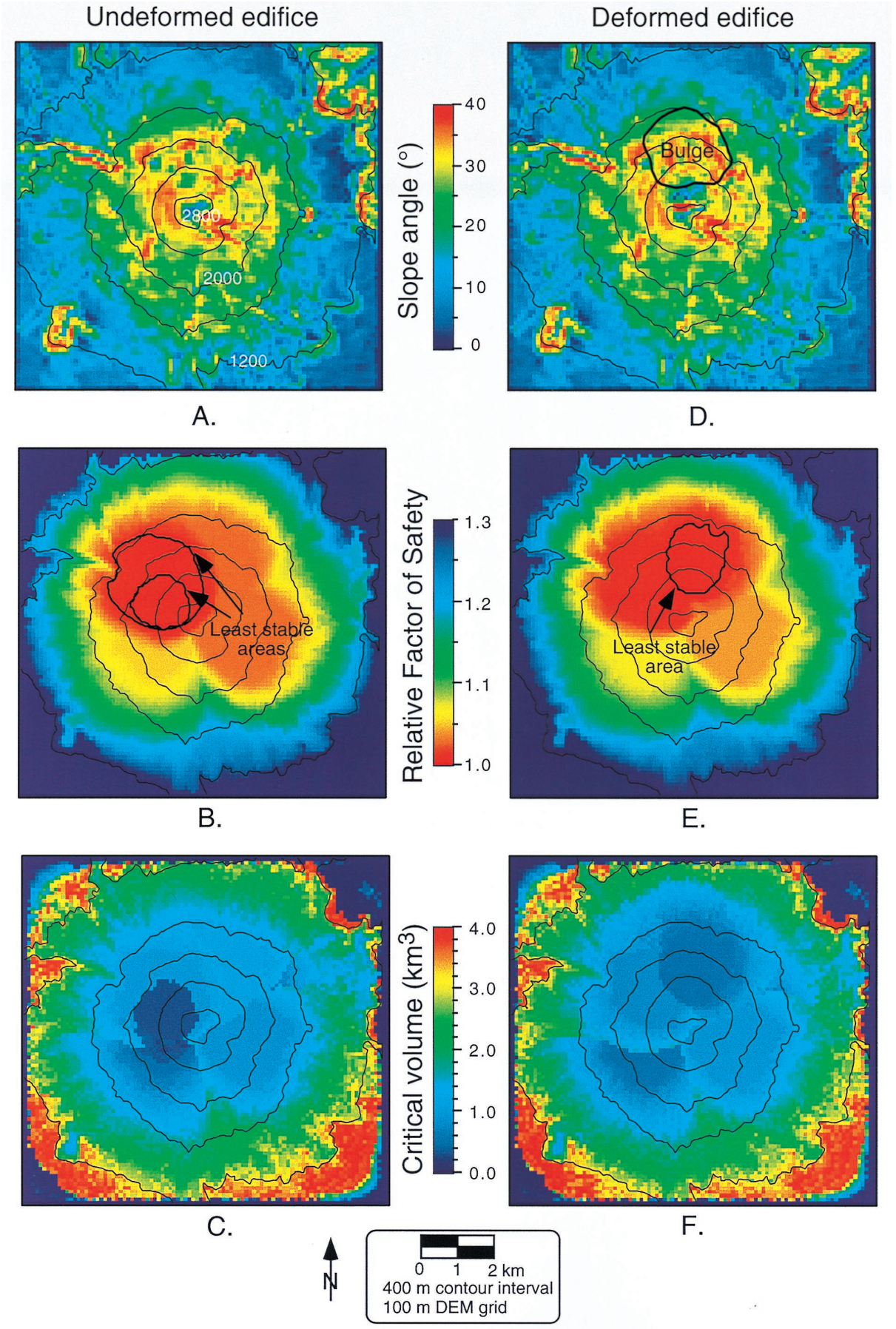
Undeformed edifice
Deformed edifice
2800
2000
1200
Bulge
Slope angle (°)
40
30
20
10
0
A.
D.
Least stable areas
Least stable area
Relative Factor of Safety
1.3
1.2
1.1
1.0
B.
E.
Critical volume (km3)
4.0
3.0
2.0
1.0
0.0
C.
F.
N
0 1 2 km
400 m contour interval
100 m DEM grid

range of volumes associated with all trial surfaces. The stability of large potential failures is integrated over large areas, and the pattern of relative stability in Plate 1b would not be directly anticipated from the ground surface slope map (Plate 1a). Instead, the pattern in Plate 1b results from the 3-D interaction between potential failure surfaces, material properties, and topography.

Initial movement directions associated with each of the critical surfaces affecting the DEM vary around the edifice. Many potential failures have an initial movement direction (defined by the direction of the critical limit-equilibrium computation) similar to the local ground slope direction (Figure 6), as might be expected for a failure moving directly down the overall topographic fall line. However, large potential failure blocks tend to dominate much of the edifice and some local regions may be affected by large potential failures with an initial motion direction that differs from the local slope direction. On some flanks, the least stable movement direction of the critical surfaces can differ 30°–60° from the local ground slope direction (Figure 6). Thus the direction of the ground surface slope may not necessarily predict the least stable movement direction of all edifice flanks.

We conducted a thorough search with a fine search grid spacing of 100 m and $\sim 29 \times 10^6$ trial failure surfaces to create Plates 1b and 1c. For this topography, comparative tests indicate that a similar map of F_{rel} could be obtained with a much coarser search of about 200,000 trial failure surfaces (horizontal search grid spacing of 400 m, vertical of 200 m). However, the distribution of volumes associated with F_{rel} is better defined with a finer search. Note that the volumes associated with critical surfaces near F_{min} (Figure 5) are larger than the lower volume limit (0.1 km^3), implying that no artificial volume constraints were placed on obtaining the critical potential failure surfaces.

4.3. Pore Pressure and Earthquake Effects

For the undeformed Mount St. Helens edifice with a pore pressure ratio of 0.3, our analyses show that F_{min} decreases to about 1.59 (Table 2). The pore pressure ratio r_u uniformly affects the frictional strength along the potential sliding surface (see equation (14)). For a potential failure surface dominated by frictional strength, the factor of safety, F, would proportionally decrease as r_u increases. *Bishop and Morgenstern* [1960] illustrated that there is a nearly linear relation between r_u and F for many sets of material parameters. Thus F_{rel} should remain essentially the same as r_u changes. For the Mount St. Helens edifice with an r_u of 0.3, the values and spatial pattern of F_{rel} remain within 1% of the dry case.

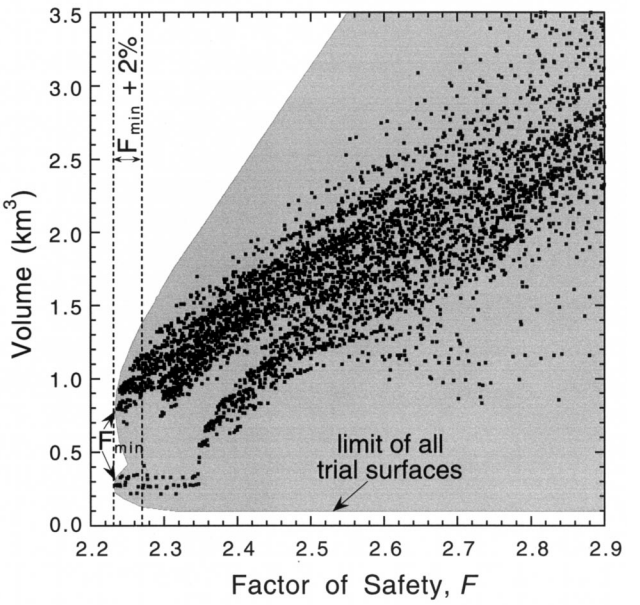

Figure 5. Factor of safety versus volume for potential failure surfaces affecting the undeformed, dry, static Mount St. Helens edifice. Points represent critical volumes portrayed in Plate 1c. Gray area defines the limit of the $\sim 29 \times 10^6$ computed trial failure surfaces.

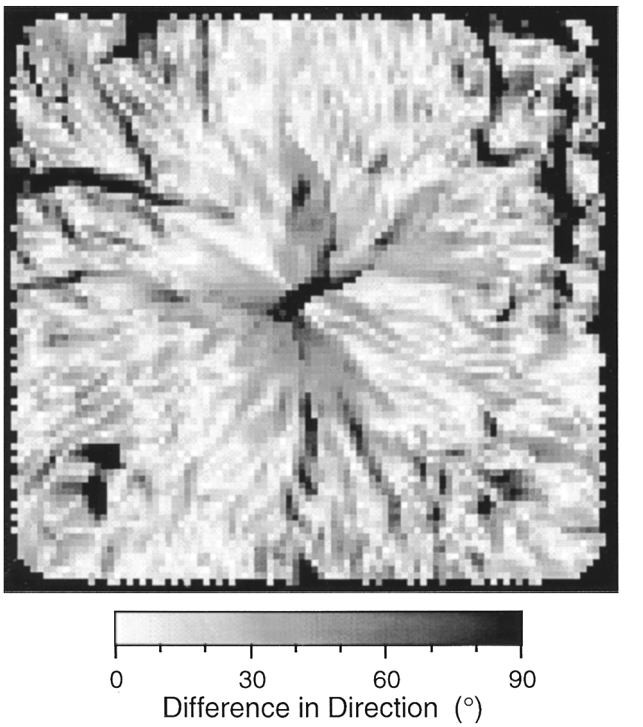

Figure 6. Difference between local ground slope direction and initial movement direction for critical failure surfaces affecting each 100-m DEM grid point for dry, static, undeformed Mount St. Helens edifice.

Plate 1. (opposite) Results for the precollapse Mount St. Helens edifice. The relative factor of safety is defined as $F_{rel} = F/F_{min}$; values of one represent areas of the lowest stability. Potential failure volumes represent the volumes associated with critical failure surfaces affecting each DEM grid point. For comparison all results use a dry, static edifice. (a) Undeformed edifice: ground surface slope from the 100-m DEM. Topographic contour interval is 400 m. (b) Undeformed edifice: relative factor of safety, F_{rel}, for each DEM grid point. Outlines of two least stable areas with $F_{rel} = 1$ are shown on the northwest flank. (c) Undeformed edifice: potential failure volumes associated with the F_{rel} values shown in Plate 1b. (d) Deformed edifice: ground surface slope from the 100-m DEM. Approximate outline of bulge prior to collapse shown on north flank. (e) Deformed edifice: relative factor of safety, F_{rel}, for each DEM grid point. Outline of least stable area with $F_{rel} = 1$ is shown on the north flank. (f) Deformed edifice: potential failure volumes associated with the F_{rel} values shown in Plate 1e.

Table 2. Computed Minimum Factor of Safety F_{min} and Critical Volume V_C for Different Scenarios at Mount St. Helens Using $\phi = 40°$ and $c = 1000$ kPa

	Scenario			
	1, Dry	2, Pore Pressure $r_u = 0.3$	3, Earthquake $k = 0.2g$	4, Pore Pressure Plus Earthquake
		Undeformed DEM Grid		
F_{min}	2.23	1.59	1.52	1.05
V_C, km^3	0.3 and 0.8	0.9	0.9	1.0
		Deformed DEM Grid		
F_{min}	2.22	NC	NC	1.05
V_C, km^3	0.4			1.1

NC, not computed.

For the dry, undeformed Mount St. Helens edifice with a uniform horizontal acceleration of $0.2g$, F_{min} decreases to ~1.52 (Table 2). The relative stability map of the upper edifice is very similar to the dry case with no earthquake shaking. Although most of the central edifice retains the same F_{rel}, the outer edges that are affected by large potential failure surfaces show up to a 10% reduction in F_{rel} (Figure 7). These results indicate that the precollapse stability of Mount St. Helens can be reduced by either a uniform pore pressure ratio or a pseudo-static earthquake shaking force. The critical volumes vary somewhat (Table 2) but are generally between 0.8 and 1.0 km^3. The precollapse relative stability, however, is not greatly affected by these additional factors. Thus the dry, static edifice F_{rel} provides a good indicator of relative instability (useful for precollapse hazard analyses), even with simplistic, uniform pore pressure effects or earthquake shaking.

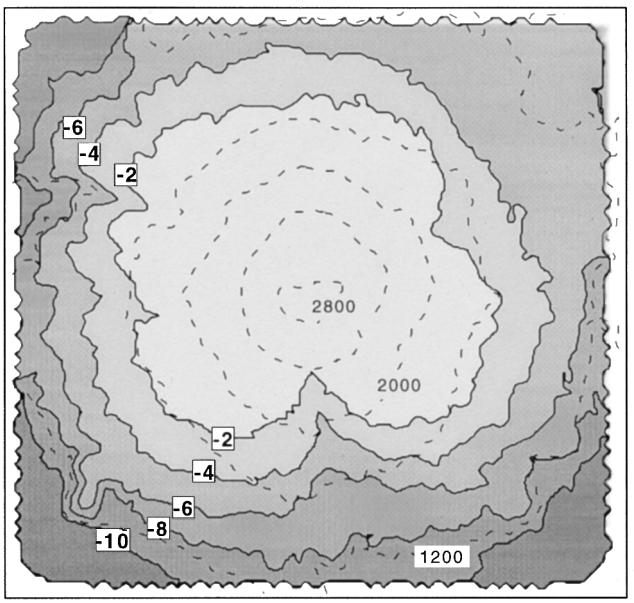

Figure 7. Percentage change in relative factor of safety, F_{rel}, induced by earthquake shaking with a horizontal acceleration of $0.2g$ compared to the dry, static, undeformed Mount St. Helens edifice. Dashed lines are 400-m topographic contours.

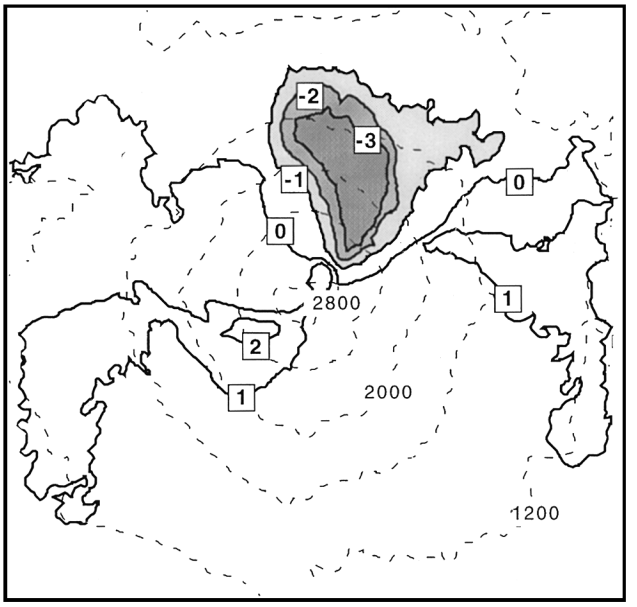

Figure 8. Percentage change in absolute factor of safety, F, between the undeformed, dry, static edifice and the deformed dry, static Mount St. Helens edifice. Dashed lines are 400-m topographic contours.

4.4. Deformed Edifice

We also examined the 3-D stability of the deformed edifice as it existed 2 days prior to catastrophic collapse. Ground surface slope derived from the deformed 100-m DEM is shown in Plate 1d. The bulge on the north flank has steeper slopes compared to the undeformed edifice, whereas the graben upslope of the bulge has gentler slopes. Given this deformed topography and dry, static conditions, an overall F_{min} of about 2.22 (Table 2) occurs in the bulge on the north flank of the edifice ($F_{rel} = 1$ in Plate 1e). However, a large region encompassing most of the north and northwest flanks has F_{rel} within a few percent of the minimum. The volume of the critical surface ($F_{rel} = 1$) is ~0.4 km^3 and most of the upper edifice contains critical volumes of <1.0 km^3 (Plate 1f). Deformation decreases the factor of safety of the north flank by ~3% over the undeformed edifice, with the largest decrease occurring in the region of the bulge (Figure 8). Given the estimated conditions present during collapse with combined $r_u = 0.3$ and $k = 0.2$ [*Voight et al.*, 1983], our method results in an F_{min} of about one and an associated potential failure volume of ~1.1 km^3 (Table 2). This large critical surface encompasses part of the bulge area and part of the edifice west of the bulge.

4.5. Effects of Uncertainty

Uncertainty in a variety of factors can affect the results of our analyses. We examined the effects of two possibilities: (1) potential inaccuracies in the limit-equilibrium computational methods and (2) potential uniform variations in rock properties. Our 3-D comparisons obtained F_{min} within ~2% of other, more rigorous methods that explicitly incorporate lateral forces, such as those presented by *Baker and Leshchinsky* [1987]. Thus our computational method may have up to 2% inaccuracy in determining F. Given that the "true" F is unknown using our methods, we could treat computational uncertainty by assuming that areas with F_{min} +2% have about equal stability. These areas have $F_{rel} \leq 1.02$ on the relative

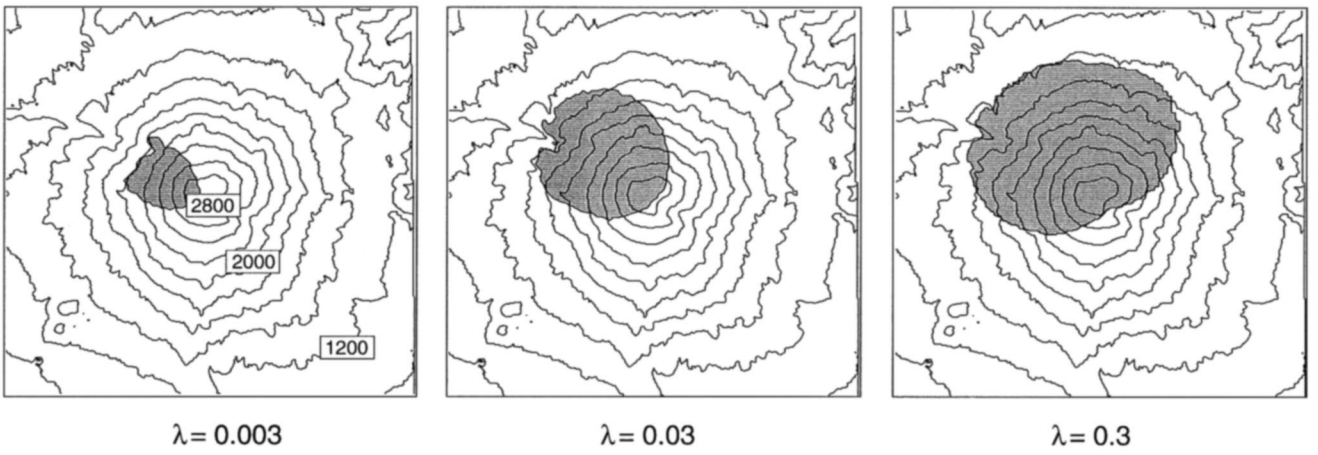

Figure 9. Regions of low stability, F_{min} +2%, with different values of λ for dry, static, undeformed Mount St. Helens edifice. Larger values of λ (more cohesion dominated) result in larger low stability areas. Topographic contour interval is 200 m.

stability maps. The potential failure volumes associated with any trial surface having F_{min} +2% for the dry, static, undeformed edifice are shown in Figure 5; they range from ~0.1 to 1.3 km^3, with a mean of ~0.7 km^3. Here, small uncertainties in F can lead to large uncertainties in potential failure volume; a variety of potential failures with widely varying volumes can have very similar factors of safety.

Another uncertainty concerns variations in material properties; the average rock properties of the Mount St. Helens edifice may have differed significantly from those used in the above analyses. Moreover, the properties probably varied significantly throughout the edifice and thus varied between potential failure surfaces. However, given that this variation was poorly known, we examined the effects of uniform variations in rock properties by varying values of λ. In general, larger values of uniform λ should lead to larger regions with low F_{rel} (see above discussion of λ effects). Using the dry, static, undeformed edifice, Figure 9 illustrates the least stable regions associated with three different values of λ; for convenience height H equals 1600 m. Each least stable region is composed of the area having $F_{rel} \leq 1.02$. Small values of λ (friction-dominated material) result in a small least stable region on the northwest side of the edifice. Large values of λ (cohesion-dominated material) result in a large least stable region encompassing much of the northwest and north flanks of the edifice. Volume limits between 0.1 and 3.5 km^3 slightly restrict the volume of the least stable critical surface with $\lambda = 0.003$ and $\lambda = 0.3$. However, least stable regions for these two cases using unrestrictive volume constraints closely resemble the regions shown in Figure 9. Cohesionless materials ($\lambda = 0$) present a special case. Given the lower constraint of 0.1 km^3, cohesionless materials produce a least stable region similar to that produced by $\lambda = 0.003$. Given an unrestrictive lower volume, critical surfaces in cohesionless materials tend to encompass small volumes and occur in areas of steep slopes. A map of F_{rel} using dry, cohesionless materials and a very small lower volume limit correlates well with the corresponding slope map.

5. Discussion

Our analysis method provides a rational and reproducible method for examining the 3-D gravitational stability of a volcano edifice. Results from such an analysis can be used to address a variety of questions including: Where is the least stable area, based on topography? For a given set of material properties, how unstable is the least stable area (i.e., what is the factor of safety)? What is the potential failure volume of the least stable area? What is the stability of any other specified part of the edifice? What are the potential failure volumes of any part of the edifice? Beyond these relatively straightforward questions, several issues arise concerning hazard analyses of stratovolcanoes: (1) What is the accuracy of our method when estimating collapse volume and location? (2) How might estimates of these quantities be used to better assess the hazards from debris avalanches or debris flows derived from edifice collapses? This discussion focuses on these issues.

In the absence of deformation or other localized volcanic unrest, a hazard analysis of Mount St. Helens would have used the undeformed edifice topography. Our analysis focuses on gravitational instability; therefore it is most applicable for estimating the size (~0.8 km^3) and location (north flank bulge) of the initial failure. Although pore pressure and earthquake shaking effects can reduce absolute stability, our results indicate that the relative stability of most of the edifice remains the same with simplistic versions of these effects. Thus a preliminary scenario where geologic conditions are relatively unknown might assume a dry, static edifice with uniform materials. Using these conditions, our analysis predicted that the least stable area existed on the northwest flank (Plate 1b). However, areas of relatively low stability also occurred on the north (within 5% of F_{min}) and southeast flanks, and most of the upper edifice stability was within 10% of F_{min}. Given the relative symmetry of the undeformed edifice, this uniformity might be anticipated. Volumes associated with the least stable areas were 0.3 and 0.8 km^3; critical volumes for most of the upper edifice ranged between 0.1 and 1.5 km^3. Although our analysis of the undeformed edifice did not predict that the least stable region would occur in the exact location of the May 18, 1980, collapse, it did indicate that the north flank was relatively unstable. Moreover, it provided estimates of potential failure volumes that bracket the actual slide block I volume. This analysis, conducted prior to volcanic unrest or catastrophic collapse, could have provided some insight into the distribution of relatively unstable areas and potential failure volumes.

However, our analysis could not have identified unconditionally stable areas, owing to poorly known geologic conditions within the edifice. Using the deformed topography with reasonable material properties, pore pressure effects, and earthquake shaking, we obtained a factor of safety near one in part of the bulge region. However, this situation would be unknown prior to deformation and thus of less use in a precollapse hazard analysis.

The relative success of topography as a predictor of unstable areas at Mount St. Helens may be due to the relative homogeneity of the precollapse edifice strength. Alternatively, because there was a series of older dome complexes deep under the north flank, this area may have been structurally predisposed to failure. Other potentially destabilizing geologic conditions within the edifice, such as locally weak materials or shallow magma injection, appear to have at least partially influenced the ultimate failure location. Nevertheless, our results indicate that an analysis of gravitational instability, even in the absence of magmatic forcing, has some predictive capability. Moreover, if the 3-D spatial variability in material properties is known or can be estimated, our method can incorporate these effects, possibly leading to better precollapse hazard analyses. We did not incorporate detailed spatial variations in our preliminary analyses because these variations are often poorly known prior to collapse.

In addition to modifying the edifice itself, large failures can result in debris avalanches or debris flows that travel far from the edifice. Clearly, our methods can suggest which drainages are most likely to experience debris avalanches or flows. Our methods can also provide important initial conditions for assessing or modeling the extent of downstream effects. For example, a frequently used approach for estimating the travel distance of a debris avalanche or flow relies on a characteristic ratio of vertical descent H_f to horizontal runout length L. Many researchers have used this H_f/L ratio to estimate the runout from large failures, and there is considerable evidence that this ratio is correlated with failure volume [*Hsü*, 1975; *Siebert*, 1984; *Voight et al*., 1985; *Hayashi and Self*, 1992]. For this approach, our method can provide estimates of both H_f and failure volume.

Slightly more complex approaches rely on scaling arguments for estimating the inundation area of debris flows [*Iverson et al*., 1998] or rock avalanches [*Dade and Huppert*, 1998] as a function of initial failure volume. Even more complex analyses of travel distance involve downstream routing of the moving mass, similar to the hydraulic routing of water floods [*Macedonio and Pareschi*, 1992; *Voight and Sousa*, 1994; *Hungr*, 1995; *Costa*, 1997; *Iverson*, 1997]; these methods require estimates of initial discharge. Although our method does not provide estimates of discharge directly, it can provide information about initial volumes that are typically needed to estimate discharge.

Our method of assessing 3-D gravitationally induced instability using topography may provide a valuable tool for general hazard assessments. However, given the geologic complexities present at many volcanoes, simplistic results cannot be used blindly. Such analyses can aid, but not necessarily replace, site-specific investigations of potential instability.

6. Conclusions

Stratovolcano flank failures, generally ranging between 0.1 and 20 km^3, pose an important hazard both on the edifice flank itself and in downslope areas. Using a 3-D slope stability analysis with spherical failure surfaces and Coulomb shear resistance, we have developed a methodology for assessing gravitationally induced failures. Our method can search the 3-D materials underlying topography (defined by a DEM) and determine the least stable areas of an edifice and the potential failure volumes associated with these areas.

Our results yield the following conclusions:

1. Even in a homogeneous slope, material properties strongly influence the depth and volume of the least stable potential failure surface. The effects of uniform material properties are reflected in λ, a dimensionless combination of the internal angle of friction, cohesion, and weight. In a homogeneous material, larger values of λ (more cohesion dominated) lead to larger potential failure volumes.

2. Both the magnitude and spatial patterns of instability are influenced by the interaction of a potential failure surface with the 3-D medium underlying topography. For large failures in complex topography, patterns of potential instability do not match patterns of local ground surface slope. The initial movement direction of large failures is often directly down the "overall" fall line. However, some regions of an edifice may be affected by large potential failures with initial motion that differs from the local slope direction. Thus local ground surface slope direction may not necessarily predict the least stable movement direction.

3. At Mount St. Helens, computing gravitational instability prior to the 1980 collapse could have provided useful, but not exact, estimates of potential future failure size and location. Using the dry, static, undeformed edifice topography of Mount St. Helens, our method delineated the northwest flank as the least stable region, although the north flank stability was within 5% of the minimum. Pore pressure and earthquake shaking effects reduced the absolute edifice stability; however, the relative stability of most of the edifice remained the same with simplistic versions of these effects. Thus dry, static conditions can represent an initial hazard analysis scenario when geologic conditions within an edifice are poorly known. Spatial variability in material properties can be incorporated if known. Using estimates of the conditions that existed two days prior to collapse, including deformed topography with a north flank bulge in combination with pore pressure and pseudo-static earthquake shaking effects, we obtained good estimates of the actual failure location and volume.

4. Large collapses typically generate debris avalanches that may mobilize into debris flows. Most physically based approaches for assessing downslope or downstream hazards from these phenomena require knowledge of the initial failure location and volume. Our method provides an aid for estimating these quantities at other volcanoes; however, it cannot replace site-specific investigations.

Notation

a vertical driving force moment arm, L.
A area of trial failure surface, L^2.
A_c area of column on the trial failure surface, L^2.
c cohesion, M/LT^2.
e horizontal driving force moment arm, L.
F factor of safety, dimensionless.
$F_{\min}$ minimum factor of safety, dimensionless.
F_{rel} relative factor of safety, dimensionless.
g magnitude of the gravitational acceleration vector, L/T^2.

H height of cone or hillside, L.
H_f height of vertical descent, L.
k fraction of g, used for computing horizontal acceleration, dimensionless.
L horizontal runout length, L.
N_z vertical component of normal force acting on the trial failure surface, ML/T^2.
P normal force acting on the trial failure surface, ML/T^2.
r radius of spherical trial failure surface, L.
r_u pore pressure ratio, dimensionless.
R resisting force moment arm, L.
S_0, S_1, S_2 surface area of vertical cross sections through a column, L^2.
S_z vertical component of the shear force acting on the trial failure surface, ML/T^2.
u pore fluid pressure, M/LT^2.
V volume of column above trial failure surface, L^3.
V_C volume of critical failure, L^3.
W weight of column above trial failure surface, M/L^2T^2.
x, y, z Cartesian coordinates, L.
α apparent dip of trial failure surface in the direction of slide movement, dimensionless.
β azimuthal angle of initial failure movement direction, dimensionless.
ϕ angle of internal friction, dimensionless.
γ_t total unit weight of rock plus fluid, M/L^2T^2.
λ combination of cohesion, friction angle, height, and weight, dimensionless.
θ true dip of trial failure surface, dimensionless.
σ_n normal stress, M/LT^2.
τ shear stress, M/LT^2.

Acknowledgments. We thank Rex Baum, Richard Iverson, Shinji Takarada, Barry Voight, and Robert Watters for helpful reviews of this manuscript.

References

Baker, R., and D. Leshchinsky, Stability analysis of conical heaps, *Soils Founda*., *27*(4), 99–110, 1987.

Baligh, M. M., and A. S. Azzouz, End effects on stability of cohesive slopes, *J. Geotech. Eng. Div. Am. Soc. Civ. Eng*., *101*(11), 1105–1117, 1975.

Beget, J. E., and J. Kienle, Cyclic formation of debris avalanches at Mount St. Augustine volcano, *Nature*, *356*(6371), 701–704, 1992.

Bishop, A. W., The use of slip circles in the stability analysis of slopes, *Geotechnique*, *5*, 7–17, 1955.

Bishop, A. W., and N. Morgenstern, Stability coefficients for earth slopes, *Geotechnique*, *10*, 129–150, 1960.

Chen, R. H., and J.-L. Chameau, Three-dimensional limit equilibrium analysis of slopes, *Geotechnique*, *32*, 31–40, 1982.

Chowdhury, R. N., and S. Zhang, Convergence aspect of limit equilibrium methods for slopes, *Can. Geotech. J*., *27*, 145–151, 1990.

Costa, J. E., Hydraulic modeling for lahar hazards at Cascades volcanoes, *Environ. Eng. Geosci*., *3*(1), 21–30, 1997.

Crandell, D. R., and D. R. Mullineaux, Technique and rationale of volcanic-hazards appraisals in the Cascade Range, northwestern United States, *Environ. Geol*., *1*, 23–32, 1975.

Crowley, J. K., and D. R. Zimbleman, Mapping hydrothermally altered rocks on Mount Rainier, Washington, with airborne visible/infrared imaging spectrometer (AVIRIS) data, *Geology*, *25*(6), 559–562, 1997.

Dade, B. W., and H. E. Huppert, Long-runout rockfalls, *Geology*, *26*(9), 803–806, 1998.

Day, S. J., Hydrothermal pore fluid pressure and the stability of porous, permeable volcanoes, in *Volcano Instability on the Earth and Other Planets*, edited by W. J. McGuire, A. P. Jones, and J. Neuberg, *Geol. Soc. Spec. Publ*., *110*, 77–93, 1996.

Dieterich, J. H., Growth and persistence of Hawaiian volcanic rift zones, *J. Geophys. Res*., *93*(B5), 4258–4270, 1988.

Duncan, J. M., State-of-the-art: Limit equilibrium and finite-element analysis of slopes, *J. Geotech. Eng*., *122*(7), 577–596, 1996.

Duncan, J. M., and S. G. Wright, The accuracy of equilibrium methods of slope stability analysis, *Eng. Geol*., *16*, 5–17, 1980.

Elsworth, D., and B. Voight, Dike intrusion as a trigger for large earthquakes and the failure of volcano flanks, *J. Geophys. Res*., *100*(B4), 6005–6024, 1995.

Environmental Systems Research Institute (ESRI), *Using ARC GRID With ARC/INFO*, vol. 1, Redlands, Calif., 1998.

Fredlund, D. G., and J. Krahn, Comparison of slope stability methods of analysis, *Can. Geotech. J*., *14*, 429–439, 1977.

Gens, A., J. N. Hutchinson, and S. Cavoundis, Three-dimensional analysis of slides in cohesive soils, *Geotechnique*, *38*, 1–23, 1988.

Glicken, H., Rockslide-debris avalanche of May 18, 1980, Mount St. Helens Volcano, Washington, *U.S. Geol. Surv. Open File Rep. 96-0677*, 1996.

Hayashi, J. N., and S. Self, A comparison of pyroclastic flow and debris avalanche mobility, *J. Geophys. Res*., *97*(B6), 9063–9071, 1992.

Hopson, C. A., and W. G. Melson, Stratigraphy of Mount St. Helens 1980 crater walls (abstract), *Eos Trans. AGU*, *63*(45), 1144, 1989.

Hoek, E., and J. W. Bray, *Rock Slope Engineering*, 3rd ed., Inst. of Min. and Metall., London, 1981.

Hovland, H. J., Three-dimensional slope stability analysis method, *J. Geotech. Eng. Div. Am. Soc. Civ. Eng*., *103*(9), 971–986, 1977.

Hsü, K. J., Catastrophic debris streams (sturzstroms) generated by rockfalls, *Geol. Soc. Am. Bull*., *86*, 129–140, 1975.

Hungr, O., An extension of Bishop's simplified method of slope stability analysis to three dimensions, *Geotechnique*, *37*, 113–117, 1987.

Hungr, O., A model for the runout analysis of rapid flow slides, debris flows, and avalanches, *Can. Geotech. J*., *32*, 610–623, 1995.

Hungr, O., F. M. Salgado, and P. M. Byrne, Evaluation of a three-dimensional method of slope stability analysis, *Can. Geotech. J*., *26*, 679–686, 1989.

Iverson, R. M., Failure and runout of giant landslides on Hawaiian volcanoes: Cases of enigmatic mechanics? (abstract), *Geol. Soc. Am. Abstr. Programs*, *23*, A125, 1991.

Iverson, R. M., Rigid-wedge models for meta-stable flanks of Hawaiian volcanoes (abstract), *Eos Trans. AGU*, *73*(43), Fall Meet. Suppl., 505, 1992.

Iverson, R. M., Can magma-injection and groundwater forces cause massive landslides on Hawaiian volcanoes?, *J. Volcanol. Geotherm. Res*., *66*, 295–308, 1995.

Iverson, R. M., The physics of debris flows, *Rev. Geophys*., *35*(3), 245–296, 1997.

Iverson, R. M., S. P. Schilling, and J. W. Vallance, Objective delineation of lahar-inundation hazard zones, *Geol. Soc. Am. Bull*., *110*(8), 972–984, 1998.

Jaeger, J. C., and N. G. W. Cook, *Fundamentals of Rock Mechanics*, 3rd ed., Chapman and Hall, New York, 1979.

Janbu, N., Stability analysis of slopes with dimensionless parameters, *Harv. Soil Mech. Ser*., *46*, 81 pp., Harv. Univ., Cambridge, Mass., 1954.

Jordan, R., and H. H. Kieffer, Topographic changes at Mount St. Helens: Large-scale photogrammetry and digital terrain models, *U.S. Geol. Surv. Prof. Pap*., *1250*, 135–141, 1981.

Kanamori, H., J. W. Given, and L. Lay, Analysis of seismic body waves excited by the Mount St. Helens eruption of May 18, 1980, *J. Geophys. Res*., *89*(B3), 1856–1866, 1984.

Lam, L., and D. G. Fredlund, A general limit equilibrium model for three-dimensional slope stability analysis, *Can. Geotech. J*., *30*, 905–919, 1993.

Lambe, T. W., and R. V. Whitman, *Soil Mechanics*, John Wiley, New York, 1969.

Lipman, P. W., J. C. Moore, and D. A. Swanson, Bulging of the north flank before the May 18 eruption: Geodetic data, *U.S. Geol. Surv. Prof. Pap*., *1250*, 143–156, 1981.

Lopez, D. L., and S. N. Williams, Catastrophic volcanic collapse: Relation to hydrothermal processes, *Science*, *260*, 1794–1796, 1993.

Macedonio, G., and M. T. Pareschi, Numerical simulations of some

lahars from Mount St. Helens, *J. Volcanol. Geotherm. Res*., *54*, 65–80, 1992.
MacLeod, N., Sector-failure eruption in Indonesian volcanoes, *Geol. Indonesia*, *12*(1), 563–601, 1989.
McGuire, W. J., Monitoring active volcanoes—An introduction, in *Monitoring Active Volcanoes: Strategies, Procedures and Techniques*, edited by W. J. McGuire, C. R. J. Kilburn, and J. Murray, pp. 1–31, UCL Press, New York, 1995.
McGuire, W. J., Volcano instability: a review of contemporary themes, in *Volcano Instability on the Earth and Other Planets*, edited by W. J. McGuire, A. P. Jones, and J. Neuberg, *Geol. Soc. Spec. Publ*., *110*, 1–23, 1996.
Miller, D. J., Coupling GIS with physical models to assess deep-seated landslide hazards, *Environ. Eng. Geosci*., *1*(3), 263–276, 1995.
Morgenstern, N. R., The evaluation of slope stability—A 25 year perspective, in *Stability and Performance of Slopes and Embankments—II*, vol. 1, edited by R. B. Seed and R. W. Boulanger, pp. 1–26, Am. Soc. of Civ. Eng., Reston, Va., 1992.
Paul, A., J. P. Gratier, and J. Boudon, A numerical model for simulating deformation of Mount St. Helens volcano, *J. Geophys. Res*., *92*(B10), 10,299–10,312, 1987.
Pierson, T. C., Hazardous hydrologic consequences of volcanic eruptions and goals for mitigative action: An overview, in *Hydrology of Disasters*, edited by O. Starosolszky and O. M. Melder, pp. 220–236, World Meteorol. Org., Geneva, 1989.
Reid, M. E., Transient thermal pressurization in hydrothermal systems: A cause of large-scale edifice collapse at volcanoes? (abstract), *Geol. Soc. Am. Abstr. Programs*, *26*, A376, 1994.
Reid, M. E., Destabilizing hydrothermal pressurization in volcanoes, paper presented at IUGG XXI General Assembly, Boulder, Colo., 1995.
Seed, H. B., and G. R. Martin, The seismic coefficient in earth dam design, *J. Soil Mech. Found. Div. Am. Soc. Civ. Eng*., *92*(SM3), 25–58, 1966.
Siebert, L., Large volcanic debris avalanches: Characteristics of source areas, deposits, and associated eruptions, *J. Volcanol. Geotherm. Res*., *22*, 163–197, 1984.
Siebert, L., Hazards of large volcanic debris avalanches and associated eruptive phenomena, in *Monitoring and Mitigation of Volcano Hazards*, edited by R. Scarpa and R. I. Tilling, pp. 541–572, Springer-Verlag, New York, 1996.
Siebert, L., H. Glicken, and T. Ui, Volcanic hazards from Bezymianny- and Bandai-type eruptions, *Bull. Volcanol*., *49*, 435–459, 1987.
Swanson, D. A., B. P. Hausback, and D. R. Zimbelman, Why was the 1980 bulge on the north flank of Mount St. Helens?, paper presented at IUGG XXI General Assembly, Boulder, Colo., 1995.
Tilling, R. I., The role of monitoring in forecasting volcanic events, in *Monitoring Active Volcanoes: Strategies, Procedures and Techniques*, edited by W. J. McGuire, C. R. J. Kilburn, and J. Murray, pp. 369–402, UCL Press, New York, 1995.
Ugai, K., Three-dimensional slope stability analysis by slice methods, in *Numerical Methods in Geomechanics*, vol. 2, edited by G. Swoboda, pp. 1369–1374, A. A. Balkema, Brookfield, Vt., 1988.
Ui, T., Volcanic dry avalanche deposits—Identification and comparison with nonvolcanic debris stream deposits, *J. Volcanol. Geotherm. Res*., *18*, 135–150, 1983.
Voight, B., Time scale for the first movements of the May 18 eruption, *U.S. Geol. Surv. Prof. Pap*., *1250*, 69–86, 1981.
Voight, B., and D. Elsworth, Failure of volcano slopes, *Geotechnique*, *47*, 1–31, 1997.
Voight, B., and J. Sousa, Lessons from Ontake-san: A comparative analysis of debris avalanche dynamics, *Eng. Geol*., *38*, 261–297, 1994.
Voight, B., R. J. Janda, H. Glicken, and P. M. Douglass, Nature and mechanics of the Mount St. Helens rockslide-avalanche of 18 May 1980, *Geotechnique*, *33*, 243–273, 1983.
Voight, B., R. J. Janda, H. Glicken, and P. M. Douglass, Discussion of nature and mechanics of the Mount St. Helens rockslide-avalanche of 18 May 1980, *Geotechnique*, *35*, 357–368, 1985.
Watters, R. J., and W. D. Delahaut, Effect of argillic alteration on rock mass stability, in *Clay and Shale Slope Instability*, *Rev. Eng. Geol*., vol. X, edited by W. C. Haneburg and S. A. Anderson, pp. 139–150, Geol. Soc. of Am., Boulder, Colo., 1995.
Whitman, R. V., and W. A. Bailey, Use of computers for slope stability analysis, *J. Soil Mech. Found. Div. Am. Soc. Civ. Eng*., *93*(SM4), 475–498, 1967.
Xing, Z., Three-dimensional stability analysis of concave slopes in plan view, *J. Geotech. Eng. Am. Soc. Civ. Eng*., *114*(6), 658–671, 1988.

D. L. Brien, S. B. Christian, and M. E. Reid, U.S. Geological Survey, MS910, 345 Middlefield Road, Menlo Park, CA 94025. (mreid@usgs.gov)

(Received January 29, 1999; revised August 30, 1999;
accepted September 2, 1999.)